nature astronomy

ARTICLES

https://doi.org/10.1038/s41550-020-1172-6

Check for updates

Magnetized filamentary gas flows feeding the young embedded cluster in Serpens South

Thushara G.S. Pillai[1,2]✉, Dan P. Clemens[1], Stefan Reissl[3], Philip C. Myers[4], Jens Kauffmann[5], Enrique Lopez-Rodriguez[6], F. O. Alves[7], G. A. P. Franco[8], Jonathan Henshaw[9], Karl M. Menten[2], Fumitaka Nakamura[10], Daniel Seifried[11], Koji Sugitani[12] and Helmut Wiesemeyer[2]

Observations indicate that molecular clouds are strongly magnetized, and that magnetic fields influence the formation of stars. A key observation supporting the conclusion that molecular clouds are significantly magnetized is that the orientation of their internal structure is closely related to that of the magnetic field. At low column densities, the structure aligns parallel with the field, whereas at higher column densities, the gas structure is typically oriented perpendicular to magnetic fields, with a transition at visual extinctions $A_V \gtrsim 3$ mag. Here we use far-infrared polarimetric observations from the HAWC+ polarimeter on SOFIA to report the discovery of a further transition in relative orientation, that is, a return to parallel alignment at $A_V \gtrsim 21$ mag in parts of the Serpens South cloud. This transition appears to be caused by gas flow and indicates that magnetic supercriticality sets in near $A_V \gtrsim 21$ mag, allowing gravitational collapse and star cluster formation to occur even in the presence of relatively strong magnetic fields.

A fundamental question in star formation physics is 'What processes create and support dense interstellar medium filaments and regulate the star formation within them?' While magnetic fields are predicted to play an important role in the formation of dense filamentary structures, of dense cores and ultimately of stars within them, the importance of magnetic fields relative to turbulence and gravity remains poorly constrained[1,2].

Dust emission polarization observations at 353 GHz by the Planck satellite have shown ordered magnetic field structures towards the Gould Belt clouds in the solar neighbourhood[3]. Studies have further quantified the importance of magnetic fields via an assessment of the relative orientation between column density (N_H) structures (filaments) and the plane of the sky magnetic field (B_{pos}). Within a star-forming complex, low-column-density features are preferentially aligned parallel to the magnetic field, while at high column density, they tend to be perpendicular to the field. A transition between the modes is observed for a visual extinction (A_V) range of ~2.7–3.5 mag (refs. [3,4]). Optical and near-infrared (NIR) dust extinction polarization observations of lower-column-density regions of filaments show similar behaviour[5–9].

Yet, the Planck satellite's ~10′ beam, which corresponds to linear scales of ~1 pc × (d/345 pc), was unable to resolve details of the magnetic field structure on dense cores size scales (<0.1 pc). The specific role of magnetic fields in shaping how the filaments fragment into cores and on to form stars and clusters thus remains unknown.

The Serpens South cloud resides in the Aquila Rift complex[10] at a distance of 436 pc (ref. [11]). Figure 1 shows that this cloud harbours a prominent hub-filament system, that is, a system of filaments that radiate from a denser hub (a zone with protostellar formation[12]). Based on its high ratio of protostellar (class 0/I) sources relative to pre-main sequence (class II/III) sources, the star cluster in the Serpens South hub is probably the youngest cluster in the local neighbourhood[10]. The extreme youth and proximity of this hub-filament system makes it an ideal laboratory for testing the role of magnetic fields in a filamentary dark cloud in an early stage of star cluster formation.

The data

Serpens South was observed using the High-resolution Airborne Wideband Camera-Plus (HAWC+) polarimeter on the 2.7 m Stratospheric Observatory for Infrared Astronomy (SOFIA) telescope, using the far-infrared (FIR) E band (with mean wavelength $\lambda_C = 214\,\mu$m, bandwidth $\Delta\lambda = 44\,\mu$m; Methods). The main data products were the fractional polarization (P), position angle (PA) and their uncertainties (σ_P, σ_{PA}).

For regions of the cloud with weak detections, it was necessary to smooth the data to achieve adequate signal-to-nose ratios in polarization (PSNR $\equiv P'/\sigma_P$), where P' is the debiased fractional polarization and σ_p its uncertainty (Methods). Radiative aligned torques (RATs)[13] cause dust grains in dense clouds to align such that their major axes, which are sensed by FIR emission polarimetry, are oriented perpendicular to the magnetic field[14]. Therefore, the HAWC+ vectors discussed throughout the text have been rotated by 90° relative to the electric field orientation to denote the plane of the sky magnetic field B_{pos}. The resultant polarization vectors are shown in Fig. 1.

The NIR extinction polarization vectors presented in Fig. 1 were adopted from literature[5], selecting their H-band data. Only polarization values that satisfied the additional quality criteria discussed in Kusune et al.[15] were considered. The NIR vectors directly sense B_{pos} and so have not been rotated.

[1]Institute for Astrophysical Research, Boston University, Boston, MA, USA. [2]Max-Planck-Institut für Radioastronomie, Bonn, Germany. [3]Universität Heidelberg, Zentrum für Astronomie, Institut für Theoretische Astrophysik, Heidelberg, Germany. [4]Harvard-Smithsonian Center for Astrophysics, Cambridge, MA, USA. [5]Haystack Observatory, Massachusetts Institute of Technology, Westford, MA, USA. [6]SOFIA Science Center, NASA Ames Research Center, Moffett Field, CA, USA. [7]Max-Planck-Institut für Extraterrestrische Physik, Garching, Germany. [8]Departamento de Física-ICEx-UFMG, Belo Horizonte, Brazil. [9]Max-Planck-Institute for Astronomy, Heidelberg, Germany. [10]National Astronomical Observatory of Japan, Tokyo, Japan. [11]Universität zu Köln, I. Physikalisches Institut, Köln, Germany. [12]Graduate School of Natural Sciences, Nagoya City University, Nagoya, Japan. ✉e-mail: tpillai.astro@gmail.com

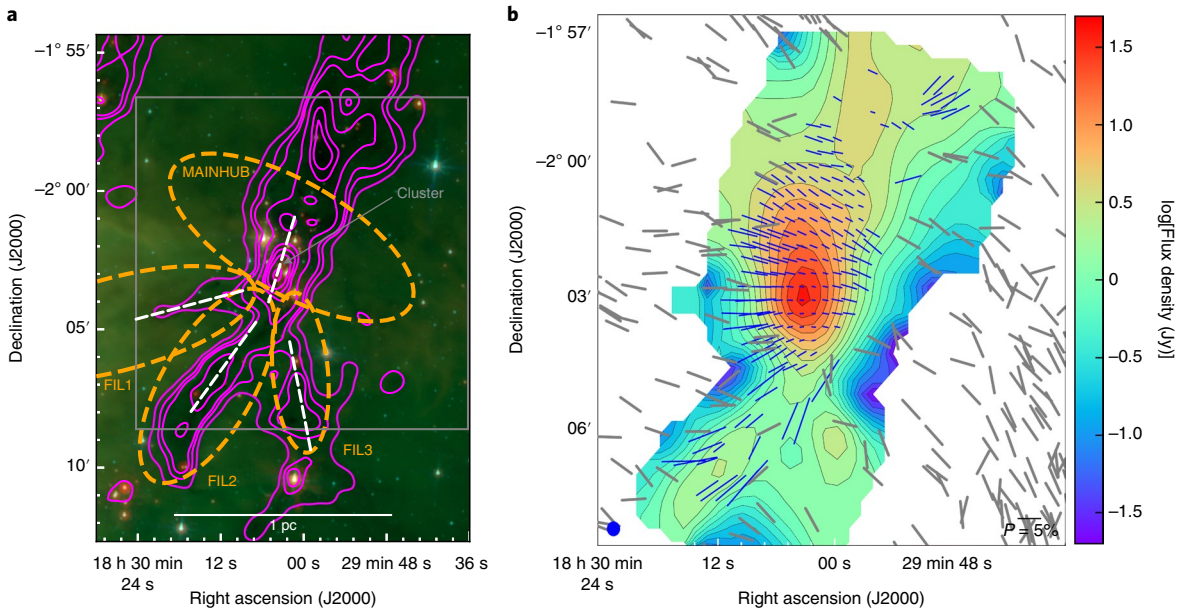

Fig. 1 | The Serpens South cloud and its magnetic field. a, Three-colour overview map generated from data acquired with the Spitzer Multiband Imaging Photometer (MIPS) 24 μm (red), Infrared Array Camera (IRAC) 8 μm (blue) and IRAC 5.8 μm (green) sensors. The grey box shows the region mapped with HAWC+, magenta contours correspond to the H_2 column densities from Herschel data[16] at A_V values of 15, 20, 30, 45, 70, 85, 110 and 150 mag, and the dashed white lines show the median RHT-traced filament orientations (see text). Orange ellipses delimit the regions containing MAINHUB, FIL1 and FIL2. White solid line of 1 pc shows a physical length scale of 3.26 light years. **b**, HAWC+ 214 μm intensity (colour scale) and polarimetry from NIR[5] (grey vectors), and HAWC+ 214 μm data (blue vectors, this work) at PSNR > 3 and PSNR > 2, respectively, tracing the magnetic field orientations, corresponding to $\sigma_{PA} < 10(14)°$. The blue circle in the bottom-left corner shows the HAWC+ 214 μm beam size. The reference percentage polarization length for HAWC+ is shown on the bottom right, while the lengths of the NIR vectors were set to be identical.

In addition, we used a Herschel gas (H_2) column density map derived by the Herschel Gould Belt Survey[16]. The map was based on Herschel 70 to 500 μm images[17] at a resolution of 36″. We used the standard conversion factor[18] between column density and visual extinction, $N_{H_2} = 9.4 \times 10^{20}$ cm^{-2} (A_V mag)$^{-1}$.

Results

Figure 1 shows the Serpens South cloud, with NIR and HAWC+ magnetic field orientations overlaid as pseudo (headless) vectors. We partitioned the sky presentation of the cloud system into a hub (MAINHUB) that harbours the Serpens South star cluster and into three filaments (FIL1, FIL2 and FIL3) that appear to connect to the hub (Fig. 1). We delineated the extents of these filament regions using ellipses. The ellipses were chosen to maximize the number of significant polarization detections for each region but to have minimal overlap between adjacent ellipse regions (Methods). The FIL3 region was removed from the remaining analysis steps as it contained too few HAWC+ polarimetric detections.

The large-scale magnetic field orientation follows a generally northeast–southwest direction that is mostly perpendicular to the gas distribution within the MAINHUB region. The magnetic field orientations with respect to the gas distributions within FIL1 and FIL2 are more complex. The large-scale magnetic field traced by NIR polarimetry is mostly perpendicular to the gas filaments. However, the magnetic field orientations seen on the smaller scales traced by the new FIR polarimetry do not appear to follow the same patterns seen on the larger, NIR-traced, scales.

We quantified the relation between cloud gas structures and magnetic fields by measuring the relative projected orientations between the filaments and the magnetic fields traced via polarimetry. We characterized the filament orientations using the Rolling Hough Transform (RHT[19]), an image processing tool that determines the orientations of linear structures (Methods). We constructed histograms of RHT angles and magnetic field orientations within the MAINHUB, FIL1 and FIL2 regions. We also calculated median RHT angles and magnetic field orientations within each elliptical region. The uncertainty on the median was calculated by dividing the standard deviation of the observed orientations by $(N-1)^{1/2}$, where N is the sample size, following Gaussian error propagation. The results are shown in Fig. 2. At the large spatial scales of the elliptical regions (0.1–0.5 pc), the NIR polarization orientations for FIL1 show a narrow distribution whose median value is 32 ± 2° offset from being parallel to the RHT-traced gas filament orientation. For FIL2, the median NIR field orientation is 73 ± 5° offset from the filament. For MAINHUB, the NIR field orientation is 95 ± 12° from the filament angle.

These offset angle values reveal that the NIR-traced magnetic field is perpendicular to the gas structures within the FIL2 and MAINHUB zones. At smaller spatial scales (<0.1 pc), however, the smoothed HAWC+ observations of the FIL2 region show magnetic field orientations closer to being parallel to the gas filament elongation (medians offset by 22 ± 3°). For MAINHUB, the large-scale perpendicular relative orientation is preserved down to the smaller, FIR-traced scales (medians offset by 87 ± 1°). Different ellipse sizes were tried and found to yield consistent results.

FIL2, the FIR-brightest southern filament connecting to the central hub (Fig. 1), thus shows a distinct change in magnetic field orientation, from being perpendicular to the moderate-column-density gas structure to being parallel to the high-column-density one. For every FIL2 NIR and FIR dust polarization detection that met our SNR criteria, we extracted the corresponding magnetic field orientation (B_{pos}) and the Herschel-based H_2 column density and converted the latter to visual extinction A_V. Fixing the filament orientation X_{FIL} to the 144° median value from Fig. 2, we computed its difference to each magnetic field orientation ($X_{B_{pos}} - X_{FIL}$). The results are summarized in Fig. 3. The figure reveals the strong, systematic change in relative orientation between the magnetic field

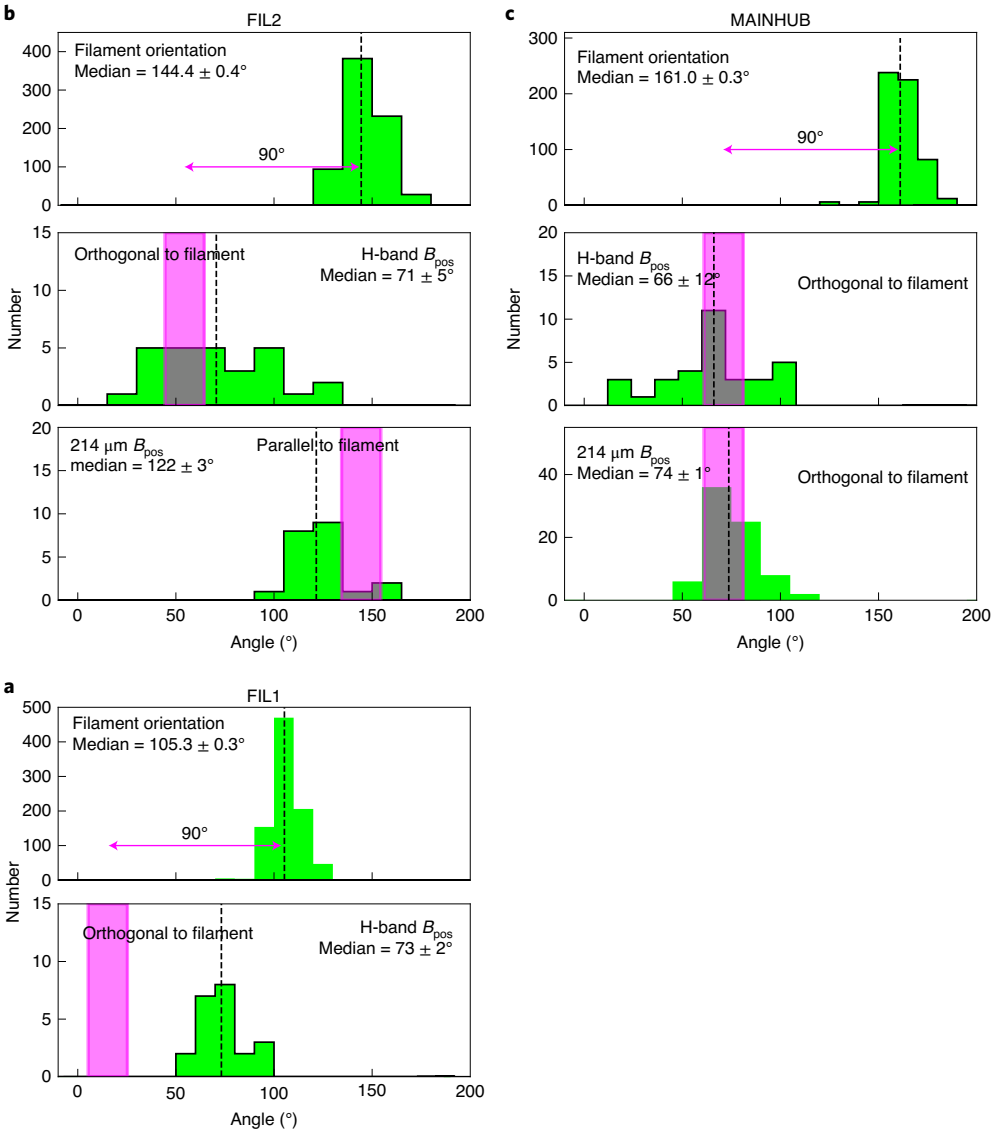

Fig. 2 | Filament and magnetic field orientations. a–c, Distributions of filament angles derived from RHT analysis (top), magnetic field orientations in the NIR (middle) and in the FIR (bottom, if present) for the FIL1 (**a**), FIL2 (**b**) and MAINHUB (**c**) elliptical regions. No HAWC+ detections have been found towards FIL1. The black dashed lines represent the medians and their uncertainties as defined in the text. The purple shaded bars represent the ranges that would conform to having either a parallel or perpendicular orientation of the field (±10°) with respect to the filament angle.

and the filament direction that occurs near an extinction threshold $A_V \approx 21$ mag.

Discussion

The results presented above can now be used to understand the role of magnetic fields in formation of the Serpens South hub-filament system.

Evidence for magnetized filamentary accretion in FIL2. At 10 arcmin resolution, Planck Collaboration Intermediate XXXV[3] found, for Gould Belt molecular clouds, a change in relative orientations between magnetic fields and filament elongations—from being generally parallel to being perpendicular—occurs at $A_V > 2.7$ mag. A similar analysis of the Aquila Rift[4], which encompasses Serpens South, found an orientation transition at $A_V \approx 3.5$ mag. These studies revealed the dynamically important role played by magnetic fields in collecting and channelling matter into present molecular cloud configurations.

The observations presented here of just such a star-forming filament show that this picture is more complex. While the perpendicular magnetic field orientation is preserved for sightlines piercing the dense hub, the moderate-column-density FIL2 region filament shows a magnetic field orientation that undergoes a change back to being parallel to the filament. The change in relative orientations between the magnetic field and the filament elongation occurs at about $A_V \approx 21$ mag, as shown in Fig. 3.

This transition threshold was determined as follows. Using 30% uncertainties for the pixels in the Herschel-based column density map, following section 4.6 of Konyves et al.[17], we binned the map pixels that matched to NIR or FIR polarization detections into logarithmically spaced bins of A_V. From the resulting distributions, we determined the first, second (median) and third quartiles for every bin. The span of the data that fell within the interquartile range, that is, within the first and the third quartile, is shown as the orange shaded region in Fig. 3. The transition threshold was taken to be where the median values of relative orientations cross 45°, namely

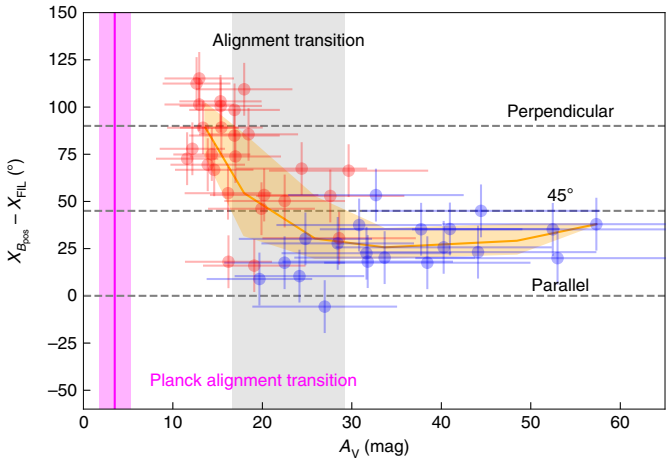

Fig. 3 | Distribution of relative orientations of the FIL2 gas filament with respect to B_{pos} as a function of A_V. The NIR B_{pos} are shown as red filled circles and the FIR as blue filled circles. Their corresponding 1σ uncertainties are shown as error bars. The three dashed lines show parallel, 45° and perpendicular orientations of the magnetic field with the filament. The orange area captures the interquartile ranges for all data versus A_V. The vertical grey rectangle highlights where the median relative orientation crosses 45°, with width related to the uncertainty of the crossing value. This indicates where the transition from a perpendicular to parallel field orientation occurs. The magenta bar represents the lower A_V, first alignment transition suggested by Planck data, for the parallel-to-perpendicular transition near $A_V \approx 3.5$ mag (ref. [4]).

21 mag. The A_V range of the transition is shown by the grey zone in the figure. It is bounded by where the first quartiles of the low A_V data points cross 45°, at 17 mag, and the where the third quartiles of the high A_V data points similarly cross that line, at 29 mag.

We interpret this changing magnetic field orientation in the FIL2 region as evidence for gravity dragging the denser gas, and entraining the frozen-in, large-scale magnetic field, to become a parallel flow of matter towards the MAINHUB region. In this interpretation, the FIL1, FIL2 and FIL3 region filaments act as accretion channels to funnel gas to the dense hub.

Numerical simulations predict that magnetic field orientations should follow such gravity-induced flows inside dense filaments[20–22]. Magnetized accretion flows had been expected and have been observed on protostellar envelope and smaller disk size scales ($\lesssim$500 au)[23–26]. Evidence for such accretion flows have been found in the smooth velocity gradients in N_2H^+ $1 \rightarrow 0$ in the FIL2 region filament[27](see also Fernández-López et al.[28]). Field-parallel orientations have been observed recently in a dense filament in Orion's OMC1 region[29] as well as in a distant, hub-filament infrared dark cloud[30]. The combined NIR and FIR polarimetric observations reported here show that filamentary accretion flows affect the local magnetic field orientation and thereby shape the magnetic field structure on filament size scales. A consistent picture emerges of a system of filaments merging into a hub via gas flows along, or entraining, magnetic field lines.

Field strengths. Magnetic field support of filaments of the FIL2 region type must lose to gravitational collapse close to where the new change in orientation has been discovered, to explain the onset of star formation. The mass-to-magnetic-flux ratio, M/Φ_B, reaches its critical value, $(M/\Phi_B)_{cr}$, and induces a filament to collapse and form stars, if $(M/\Phi_B) > (M/\Phi_B)_{cr}$ (the magnetically supercritical condition). Following McKee and Ostriker[31], and recast into typical physical units (for example, ref. [32])

$$\frac{(M/\Phi_B)}{(M/\Phi_B)_{cr}} \approx 0.76 \left(\frac{\langle N_{H_2} \rangle}{10^{23}\ \mathrm{cm}^{-2}}\right)\left(\frac{B_{tot}}{1\ \mathrm{mG}}\right)^{-1}. \quad (1)$$

For a transition at $A_V \approx 21$ mag, $(M/\Phi_B)/(M/\Phi_B)_{cr} \geq 1$ is fulfilled if $B_{tot} \leq 140\,\mu$G.

We adopted a spheroidal density distribution and assumed flux-freezing[33,34] to obtain an estimate of the magnetic field strength for the MAINHUB region. These assumptions fully constrain the relative geometry of the density distribution and the magnetic field, but not their absolute scaling. We assumed that the dense core is magnetically supercritical within the $A_V \approx 40$ mag contour (column density $\sim 4 \times 10^{22}$ cm^{-2}), where the central core becomes prominent relative to the surrounding material. This additional constrain fixes the distribution of density and magnetic field in absolute terms, resulting in a central magnetic field strength of ~870 μG and a central density of $\rho_0 = 6.3 \times 10^5$ cm^{-3} for the MAINHUB core in Serpens South.

This field strength estimate may be compared with values obtained from the empirical relation[1], $B = B_0 (n_{H_2}/10^4\ \mathrm{cm}^{-3})^{0.65}$ with $B_0 \lesssim 150\,\mu$G, and n_{H_2} is the H_2 particle density. For the FIL2 region filament, we obtained a density estimate of 6.4×10^4 cm^{-3}, appropriate for the transition at $A_V \approx 21$ mag, through dividing the Herschel column density values there by an approximate filament width[35] of ~0.1 pc. Under these assumptions, the Crutcher relation suggests $B \lesssim 500\,\mu$G, consistent with the 140 μG value obtained assuming magnetic supercriticality for the filament. For the MAINHUB region, the Crutcher relation suggests $B \lesssim 2$ mG at the modelled central density of 6.3×10^5 cm^{-3}, while we estimated 870 μG from flux-freezing.

That our estimates of B are consistent with those suggested by the Crutcher relation is remarkable, because our investigation probed (in particular in FIL2) gas that is less disturbed by star formation than the regions from which the Crutcher relation was derived (that is, traced by masers and CN emission connected to very active star formation), and thus potentially more representative of the initial conditions for star formation.

Effects of protostellar radiation on fractional polarization. While the mean magnetic field is well ordered along the northeast–southwest direction, the FIR polarized fraction is not uniform in the MAINHUB region, where the greatest number of HAWC+ polarization detections are present. A significant decrease in the polarization degree is evident in Fig. 1 towards the brightest emission peak in MAINHUB.

In Fig. 4, we show the debiased polarization fraction as a function of the FIR 214 μm total intensity (Stokes I) and the weighted least squares power-law fit to the data. We do not apply any signal-to-noise cut-offs for the fractional polarization. This is because polarization fraction is a positive quantity, and follows a Rice distribution and therefore would introduce a bias to high polarization values in regions with low PSNR[36]. We derive a best-fit power-law slope of $b = -0.55 \pm 0.03$.

A relatively wide range in this slope has been recently reported, with $b = -0.34$ towards the externally illuminated Ophiuchus A region[37], while starless cores such as Pipe 109/FeSt I-457 show[38,39] $b \approx -1$. In well-illuminated regions of molecular clouds, dust grains align with their minor axes parallel to the local magnetic field direction. However, because radiation does not sufficiently penetrate the denser parts of clouds, the efficiency of the alignment with the local magnetic field may fall substantially (see review by Andersson et al.[14]). The observed slope of $b \approx -0.5$ in Serpens South is thus intermediate between the two extreme cases: strong radiation inducing perfect dust grain alignment and weak radiation causing no alignment. The intermediate value for our slope suggests that while the efficiency of grain alignment decreases linearly with increasing optical depth, FIR polarimetry still probes the magnetic

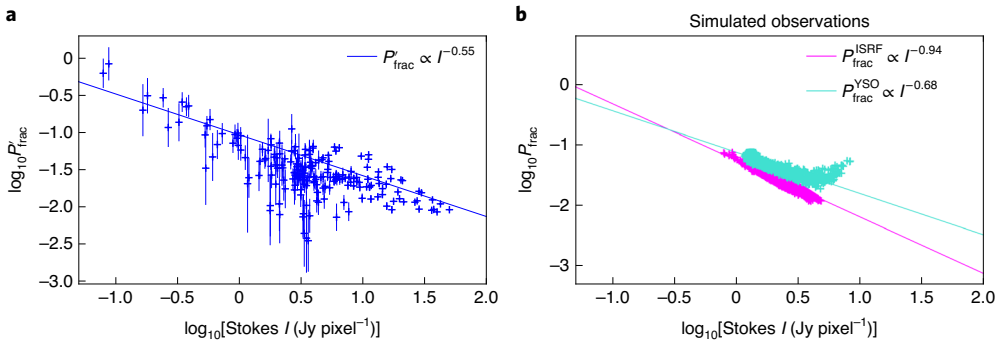

Fig. 4 | Debiased polarization fraction as a function of the total intensity. a,**b**, Comparison of the correlation between fractional polarization and column density towards MAINHUB in Serpens South using HAWC+ 214 μm (**a**) and in simulated data (**b**). P'_{frac} is the debiased fractional polarization from observations and P_{frac} is the fractional polarization. Observational uncertainties are defined in Methods. The solid line in **a** shows a least squares fit. Simulated observations from POLARIS in **b** were conducted with an ISRF alone (setup A, magenta crosses) and including the effect of a cluster of YSOs (setup B, turquoise crosses). The corresponding best fits to the model predictions are also shown.

Table 1 | Observations log

Position	Right ascension (J2000)	Declination (J2000)	Dither positions	Time on-source (s)	Chop throw (″)	Chop angle (° E of N)
1	18 h 29 min 58.54 s	−01° 59′ 49.20″	7	560	300	50
2	18 h 30 min 07.75 s	−02° 05′ 22.10″	4	320	500	60

field in the densest parts of this cloud. This is a rather surprising result given the high extinction towards the centre of the Serpens South cluster, of the order $A_V \approx 150$ mag.

To probe the nature of the alignment in more detail, we modelled the FIR dust polarization observations, based on the known properties of the cloud's density profile, its temperature and its star-formation state, as described in Methods. The modelling used the radiative transfer code POLARIS[40] to create simulated maps of dust temperature, RATs and dust polarization for two setups. Setup 'A' used an external diffuse interstellar radiation field (ISRF) as the only radiation source for dust heating and grain alignment. Setup 'B' included the ISRF as well as internal sources of radiation from the protostars in the Serpens South star cluster (Methods).

The resulting correlations between polarization fraction P_{frac} and Stokes I are shown in Fig. 4. Setup A shows a steeper slope because the external ISRF is extincted with increasing optical depth into the filament, causing the dust alignment efficiency to decrease with A_V or Stokes I. In setup B, the radiation from the embedded young stellar objects (YSOs) increases the dust alignment in the cloud core centre, leading to a shallower slope in the figure. The slope for our observations agrees better with the setup B model than with the setup A one. At the greater A_V (Stokes I) end of Fig. 4b, the setup B distribution shows a rise in fractional polarization, consistent with the localized influence of internal illumination on grain alignment at the centre of the cluster. However, this trend is not resolved in our FIR data. In summary, embedded YSOs can cause a relatively shallow slope for the correlation, consistent with our FIR observations.

Conclusions

Large-scale Planck observations of Gould Belt clouds find a transition in relative orientation between magnetic fields and gas filaments from being parallel for $A_V \leq 2.7-3.5$ mag to being perpendicular beyond that A_V range. Recent submillimetre observations show magnetic field orientations parallel to dense filaments in a few star-forming regions[29,30], but found no new transition.

The Serpens South cloud is a dense, cluster-forming, hub-filament system in the Aquila complex where we have used the HAWC+ FIR polarimeter instrument on SOFIA, in conjunction with published NIR polarimetry, to discover a new transition occurring at even greater A_V values. This new transition reveals the change of the magnetic field from being perpendicular to a large-scale, modest A_V, filament gas structure to becoming a smaller-scale magnetic field that is parallel to the densest gas structure beyond $A_V \approx 20$ mag. In addition, the slope of the observed decrease in fractional polarization with A_V is better modelled when the external ISRF is augmented by inclusion of illumination from the embedded protostars in the Serpens South cluster, enhancing the link of magnetic fields traced by FIR polarimetry with the dense, opaque gas.

This favours a scenario of gas filaments merging into a central hub, reorienting or entraining the magnetic field in the dense gas flows. Recent kinematic observations show evidence for gas flows along such filaments towards the hub in systems, including in Serpens South[27,41,42]. Thus, at the <0.1 pc scale, we find observational evidence for the feeding of gas, containing significant magnetic fields, into a low-mass, cluster-forming region.

Methods

Observations. As part of the ongoing POLSTAR (POLarization in STAR forming filament) survey, Serpens South was observed (principal investigator, Pillai; ID, 05_0206) on 12–13 May 2017 using HAWC+[43–45] with the 2.7 m SOFIA telescope. HAWC+ polarimetric observations simultaneously imaged two orthogonal components of linear polarization onto two detector arrays of up to 32×40 pixels each. Observations performed using the E band provided a pixel scale of 9.37″, a beam size of 18.2″ and an instantaneous field-of-view of up to 4.2×6.2 arcmin^2.

Observations were conducted using the standard chop-nod polarimetric mode. Specifically, a four-position dither pattern with an offset of three pixels (28″) was used. At each dither position, a halfwave plate stepped through four distinct position angles, and images were obtained at each step. Observations used nod times of 40 s, with a chop frequency of 10.2 Hz. Final polarimetric images were composed from observations of two different sky pointing directions, as listed in Table 1. The total on-source time was 880 s. Based on the morphology of the source from Herschel observations, chopping did not switch into substantial flux contribution from diffuse extended emission or compact sources.

The data were reduced using HAWC_DRP pipeline v1.3.0 and custom Python routines. Detailed data reduction steps can be found in Harper et al.[45]. In summary, the raw data were demodulated, chop-nod and background subtracted, flux calibrated, and Stokes parameters (I, Q and U) were estimated along with

their uncertainties. Fractional polarization (P), position angle (PA) and their uncertainties were evaluated using equations (1), (2), (4) and (5) of Gordon et al.[46]. The final P and PA were corrected using measured instrumental polarizations and were then debiased. The debiased fractional polarization was derived from the fractional polarization as[47] $P' = \sqrt{(P^2 - \sigma_P^2)}$.

For regions of the cloud with weak detections (for example, FIL2), it was necessary to smooth the polarization data to increase PSNR. The smoothing followed the approach detailed in Clemens et al.[48]. From a variety of trial smoothing beams, we chose a Gaussian kernel full-width at half-maximum of 18.2″ (~4 HAWC+ pixels) to smooth the SOFIA-delivered Stokes QI, UI and I maps. This yielded a maximum number of independent synthetic pixels with PSNR > 2.0 ($\sigma_{PA} < 14°$).

The NIR H-band data were adopted from Sugitani et al.[5]. Only values that satisfied the following criteria were extracted: $P/\sigma_P > 3.0$ and $P'/3 < P < 3P'$, where $P' = 2.73([H-Ks] - 0.2)$ is the best-fit colour dependence for H-band stars with $\sigma_P < 0.3\%$, following Kusune et al.[15].

Measuring filament orientations. We quantified the relationships between cloud structures and magnetic fields by measuring their relative projected orientations. To characterize filament orientations, we used the RHT[19].

The regions containing the Serpens South filaments were delimited by ellipses. These ellipses were chosen to maximize the numbers of significant polarization detections contained within each while minimizing overlap between adjacent ellipses. Since the MAINHUB gas appears in relative isolation, there is little confusion with neighbouring (FIL) ellipses. For it, we established a large encompassing ellipse that extends well beyond the high-column-density material in MAINHUB. This ensures that many NIR detections are contained in that zone. Narrower ellipses were chosen for FIL1 and FIL2 to avoid overlaps. Note that ellipse long-axis orientations are not meant to represent filament or hub gas structure elongations. The ellipses merely define regions of interest associated with the dominant gas structures contained within their boundaries.

To find linear structures in images and to determine their orientations, RHT uses three input parameters. Following the convention in Clark et al.[19], these are a smoothing kernel diameter (D_K), a diameter of the window used to roll across the image (D_W) and an intensity threshold (Z) above which data are extracted. Our input image was the Herschel dust column density map. Our choices of RHT parameters were $D_K = 55$ pixels (5.7 arcmin), $D_W = 15$ pixels (1.5 arcmin) and $Z = 70\%$ of the map peak intensity. We explored input variable values and found a wide combination of values still extracted the same filaments, ensuring robust results.

Flux-freezing model. The Serpens South cloud harbours a centrally condensed core whose surrounding polarization directions suggest the ordered pattern expected for flux-freezing[34] combined with a random component that may be attributed to turbulent motions. To estimate the maximum magnetic field strength associated with the star-forming Serpens South core, we assumed that the core is magnetically supercritical within the $A_V \approx 40$ mag contour (column density $\approx 4 \times 10^{22}$ cm^{-2}), which is where the core appears to emerge from its harbouring filament. The field strength was obtained from the flux-freezing model[33,34], and from a model of the core as prolate spheroid[49].

The core density model was obtained by fitting $p = 2$ Plummer[50] column density profiles (consistent with the cloud structure[17]) to the principal axes of the Herschel-based core column density map shown in Fig. 1. This modelling gave a central volume density $\rho_0 = 6.3 \times 10^5$ cm^{-3} and scale length $R_{flat} = 0.03$ pc. These parameters were used to obtain expressions for the core volume density and mean volume density, per Myers et al.[34].

Then, as shown in Myers et al.[34], the peak field strength in the core equatorial plane can be expressed as

$$B_0 = \left[(8\pi/3)\ G^{1/2}\ \rho_0\ r_0\right]\left[3(\xi_c - \arctan \xi_c)\right]^{1/3}\ , \qquad (2)$$

where G is the gravitational constant, r_0 is the scale length, x_c is the radius of the $A_V \approx 40$ mag map contour and $\xi_c = x_c/r_0$ is the dimensionless radius. For Serpens South, we found $\xi_c = 2$. Evaluating equation (2) yielded $B_0 = 0.87$ mG, which serves better than an order-of-magnitude estimate, based on the assumption of the core being magnetically supercritical within the $A_V \approx 40$ mag contour. This estimate is useful, but we caution that it harbours ill-constrained, difficult to quantify uncertainties.

Radiative transfer using POLARIS. We used the radiative transfer code POLARIS[40] to create simulated dust temperature, RATs and dust polarization maps on a cylindrical grid. The cylindrical grid had a length of 1 pc and a maximum radius of 0.5 pc. We applied a Plummer density profile $\rho(r) = \rho_0[1 + (r/R_{flat})^2]^{-p/2}$ with parameters $R_{flat} = 0.03$pc and $p = 2$, from the previous section.

The density ρ_0 was chosen, upon line of sight integration, to match the observed central column density of $N_{H_2} = 1.6 \times 10^{23}$ cm^2. This resulted in a total gas mass of $M_{gas} = 518\,M_\odot$ within the grid. The magnetic field was assumed to penetrate perpendicular to the spine of the cylinder, with a constant strength of $B = 100$ μG. The gas temperature was a free parameter, set initially at $T_{gas} = 15$ K to encompass the upper limit of the measured gas temperature from NH_3 observations[51].

For the dust properties, we used pre-calculated values of oblate grains with typical composition of 62.5% graphite and 37.5% silicate[52], an aspect ratio of 1:2 and a mass ratio of $M_{dust}/M_{gas} = 0.01$. The grain size a distribution followed $n(a) \propto a^{-3.5}$ with cut-offs at $a_{min} = 5$ nm and $a_{max} = 500$ nm, typical for dense clouds (for example, ref. [53]).

We conducted two different radiative transfer simulation setups to calculate grain alignment efficiencies, following RAT theory (see ref. [40]).

For setup A, an external, diffuse ISRF[54] was the only radiation source. For setup B, the luminosities and effective temperatures of the 37 Serpens South class I YSOs reported[55] were included, in addition to the ISRF. The simulated stars were placed randomly along the axial extent of the model cylinder, while their radial offsets from the spine were drawn randomly from a Gaussian distribution with a full-width at half-maximum of 0.015 pc. The latter was adopted to be bounded by the stellar surface density distribution measured by Gutermuth et al.[10]. Setup A resulted in a range of final dust temperatures, up to $T_{dust} = 20$ K at the edge of the filament model and about $T_{dust} = 8$ K towards the spine. Regarding the RATs, dust grains larger than $a = 181$ nm were well aligned to the local magnetic field when close to the filament's surface, whereas even the largest grains were not well aligned at the location of the cylinder spine. The setup B YSOs brought RATs alignment to $a = 125$ nm in the close proximity of the YSOs. Finally, we simulated synthetic polarization maps as being projected onto a detector with 64 × 64 pixels in a distance of 436 pc convolved with a beam of 19 arcsec.

Data availability

The HAWC+ data that support the plots within this paper and other findings of this study are available from the SOFIA data archive at https://dcs.arc.nasa.gov/dataRetrieval/SearchScienceArchiveInfo.jsp under project code 05_0206 or from the corresponding author upon reasonable request.

Code availability

The source code for POLARIS and PolarisTools used in this paper and written by S.R. are publicly available at http://www1.astrophysik.uni-kiel.de/polaris/.

Received: 30 September 2019; Accepted: 6 July 2020;
Published online: 17 August 2020

References

1. Crutcher, R. M. Magnetic fields in molecular clouds. *Annu. Rev. Astron. Astrophys.* **50**, 29–63 (2012).
2. Li, H.-B. et al. in *Protostars and Planets VI* (eds Beuther, H. et al.) 101–123 (Univ. Arizona Press, 2014).
3. Planck Collaboration et al. Planck intermediate results. XXXV. Probing the role of the magnetic field in the formation of structure in molecular clouds. *Astron. Astrophys.* **586**, A138 (2016).
4. Soler, J. D. et al. The relation between the column density structures and the magnetic field orientation in the Vela C molecular complex. *Astron. Astrophys.* **603**, A64 (2017).
5. Sugitani, K. et al. Near-infrared-imaging polarimetry toward Serpens South: revealing the importance of the magnetic field. *Astrophys. J.* **734**, 63 (2011).
6. Palmeirim, P. et al. Herschel view of the Taurus B211/3 filament and striations: evidence of filamentary growth? *Astron. Astrophys.* **550**, A38 (2013).
7. Franco, G. A. P. & Alves, F. O. Tracing the magnetic field morphology of the Lupus I molecular cloud. *Astrophys. J.* **807**, 5 (2015).
8. Santos, F. P., Busquet, G., Franco, G. A. P., Girart, J. M. & Zhang, Q. Magnetically dominated parallel interstellar filaments in the infrared dark cloud G14.225-0.506. *Astrophys. J.* **832**, 186 (2016).
9. Soler, J. D. Using Herschel and Planck observations to delineate the role of magnetic fields in molecular cloud structure. *Astron. Astrophys.* **629**, A96 (2019).
10. Gutermuth, R. A. et al. The Spitzer Gould Belt Survey of large nearby interstellar clouds: discovery of a dense embedded cluster in the Serpens-Aquila Rift. *Astrophys. J. Lett.* **673**, L151–L154 (2008).
11. Ortiz-León, G. N. et al. Gaia-DR2 confirms VLBA parallaxes in Ophiuchus, Serpens, and Aquila. *Astrophys. J. Lett.* **869**, L33 (2018).
12. Myers, P. C. Filamentary structure of star-forming complexes. *Astrophys. J.* **700**, 1609–1625 (2009).
13. Lazarian, A. & Hoang, T. Radiative torques: analytical model and basic properties. *Mon. Not. R. Astron. Soc.* **378**, 910–946 (2007).
14. Andersson, B.-G., Lazarian, A. & Vaillancourt, J. E. Interstellar dust grain alignment. *Annu. Rev. Astron. Astrophys.* **53**, 501–539 (2015).
15. Kusune, T. et al. Magnetic field structure in Serpens South. *Publ. Astron. Soc. Jpn* **17**, S5 (2019).
16. André, P. et al. From filamentary clouds to prestellar cores to the stellar IMF: initial highlights from the Herschel Gould Belt Survey. *Astron. Astrophys.* **518**, L102 (2010).
17. Könyves, V. et al. A census of dense cores in the Aquila cloud complex: SPIRE/PACS observations from the Herschel Gould Belt Survey. *Astron. Astrophys.* **584**, A91 (2015).

18. Kauffmann, J., Bertoldi, F., Bourke, T. L., Evans, N. J. I. I. & Lee, C. W. MAMBO mapping of Spitzer c2d small clouds and cores. *Astron. Astrophys.* **487**, 993–1017 (2008).
19. Clark, S. E., Peek, J. E. G. & Putman, M. E. Magnetically aligned H I fibers and the Rolling Hough Transform. *Astrophys. J.* **789**, 82 (2014).
20. Körtgen, B. & Banerjee, R. Impact of magnetic fields on molecular cloud formation and evolution. *Mon. Not. R. Astron. Soc.* **451**, 3340–3353 (2015).
21. Gómez, G. C., Vázquez-Semadeni, E. & Zamora-Avilés, M. The magnetic field structure in molecular cloud filaments. *Mon. Not. R. Astron. Soc.* **480**, 2939–2944 (2018).
22. Li, P. S., Klein, R. I. & McKee, C. F. Formation of stellar clusters in magnetized, filamentary infrared dark clouds. *Mon. Not. R. Astron. Soc.* **473**, 4220–4241 (2018).
23. Sadavoy, S. I. et al. Dust polarization toward embedded protostars in Ophiuchus with ALMA. II. IRAS 16293-2422. *Astrophys. J.* **869**, 115 (2018).
24. Maury, A. J. et al. Magnetically regulated collapse in the B335 protostar? I. ALMA observations of the polarized dust emission. *Mon. Not. R. Astron. Soc.* **477**, 2760–2765 (2018).
25. Takahashi, S. et al. ALMA high angular resolution polarization study: an extremely young class 0 source, OMC-3/MMS 6. *Astrophys. J.* **872**, 70 (2019).
26. Le Gouellec, V. J. M. et al. Characterizing magnetic field morphologies in three Serpens protostellar cores with ALMA. *Astrophys. J.* **885**, 106 (2019).
27. Kirk, H. et al. Filamentary accretion flows in the embedded Serpens South protocluster. *Astrophys. J.* **766**, 115 (2013).
28. Fernández-López, M. et al. CARMA Large Area Star Formation Survey: observational analysis of filaments in the Serpens South molecular cloud. *Astrophys. J. Lett.* **790**, L19 (2014).
29. Monsch, K. et al. Dense gas kinematics and a narrow filament in the Orion A OMC1 region using NH_3. *Astrophys. J.* **861**, 77 (2018).
30. Liu, T. et al. A holistic perspective on the dynamics of G035.39-00.33: the interplay between gas and magnetic fields. *Astrophys. J.* **859**, 151 (2018).
31. McKee, C. F. & Ostriker, E. C. Theory of star formation. *Annu. Rev. Astron. Astrophys.* **45**, 565–687 (2007).
32. Pillai, T. et al. Magnetic fields in high-mass infrared dark clouds. *Astrophys. J.* **799**, 74 (2015).
33. Mestel, L. The magnetic field of a contracting gas cloud. I. Strict flux-freezing. *Mon. Not. R. Astron. Soc.* **133**, 265–284 (1966).
34. Myers, P. C., Basu, S. & Auddy, S. Magnetic field structure in spheroidal star-forming clouds. *Astrophys. J.* **868**, 51 (2018).
35. Hill, T. et al. Resolving the Vela C ridge with P-ArTéMiS and Herschel. *Astron. Astrophys.* **548**, L6 (2012).
36. Montier, L. et al. Polarization measurement analysis. II. Best estimators of polarization fraction and angle. *Astron. Astrophys.* **574**, A136 (2015).
37. Pattle, K. et al. JCMT BISTRO Survey observations of the Ophiuchus molecular cloud: dust grain alignment properties inferred using a Ricean noise model. *Astrophys. J.* **880**, 27 (2019).
38. Alves, F. O. et al. On the radiation driven alignment of dust grains: detection of the polarization hole in a starless core (corrigendum). *Astron. Astrophys.* **574**, C4 (2015).
39. Kandori, R. et al. Distortion of magnetic fields in a starless core. V. Near-infrared and submillimeter polarization in FeSt 1-457. *Astrophys. J.* **868**, 94 (2018).
40. Reissl, S., Wolf, S. & Brauer, R. Radiative transfer with POLARIS. I. Analysis of magnetic fields through synthetic dust continuum polarization measurements. *Astron. Astrophys.* **593**, A87 (2016).
41. Schneider, N. et al. Dynamic star formation in the massive DR21 filament. *Astron. Astrophys.* **520**, A49+ (2010).
42. Peretto, N. et al. Global collapse of molecular clouds as a formation mechanism for the most massive stars. *Astron. Astrophys.* **555**, A112 (2013).
43. Vaillancourt, J. E. et al. Far-infrared polarimetry from the Stratospheric Observatory for Infrared Astronomy. In *Proc. SPIE, Vol. 6678, Infrared Spaceborne Remote Sensing and Instrumentation* (ed Strojnik-Scholl, M.) 66780D (SPIE 2007).
44. Dowell, C. D. et al. HAWCPol: a first-generation far-infrared polarimeter for SOFIA. In *Society of Photo-Optical Instrumentation Engineers (SPIE) Conference Series* Vol. 7735, 77356H (SPIE, 2010).
45. Harper, D. A. et al. HAWC+, the far-infrared camera and polarimeter for SOFIA. *J. Astron. Instrum.* **7**, 1840008 (2018).
46. Gordon, M. S. et al. SOFIA Community Science I: HAWC+ polarimetry of 30 Doradus. Preprint at http://arXiv.org/abs/1811.03100 (2018).
47. Serkowski, K. in *Methods in Experimental Physics* Vol. 12 (ed Carleton, N.) 361–414 (Academic Press, 1974).
48. Clemens, D. P. et al. Magnetic field uniformity across the GF 9-2 YSO, L1082C dense core, and GF 9 filamentary dark cloud. *Astrophys. J.* **867**, 79 (2018).
49. Myers, P. C. Star-forming filament models. *Astrophys. J.* **838**, 10 (2017).
50. Plummer, H. C. On the problem of distribution in globular star clusters. *Mon. Not. R. Astron. Soc.* **71**, 460–470 (1911).
51. Friesen, R. K., Bourke, T. L., Di Francesco, J., Gutermuth, R. & Myers, P. C. The fragmentation and stability of hierarchical structure in Serpens South. *Astrophys. J.* **833**, 204 (2016).
52. Reissl, S., Seifried, D., Wolf, S., Banerjee, R. & Klessen, R. S. The origin of dust polarization in molecular outflows. *Astron. Astrophys.* **603**, A71 (2017).
53. Martin, P. G. & Whittet, D. C. B. Interstellar extinction and polarization in the infrared. *Astrophys. J.* **357**, 113 (1990).
54. Mathis, J. S., Mezger, P. G. & Panagia, N. Interstellar radiation field and dust temperatures in the diffuse interstellar matter and in giant molecular clouds. *Astron. Astrophys.* **500**, 259–276 (1983).
55. Dunham, M. M. et al. Young stellar objects in the Gould Belt. *Astrophys. J. Suppl. Ser.* **220**, 11 (2015).

Acknowledgements

Based in part on observations made with the NASA/DLR Stratospheric Observatory for Infrared Astronomy (SOFIA). SOFIA is jointly operated by the Universities Space Research Association, Inc. (USRA), under NASA contract NAS2-97001, and the Deutsches SOFIA Institut (DSI) under DLR contract 50 OK 0901 to the University of Stuttgart. Financial support for this work was provided to T.P. by DLR through award number 50 OR 1719. D. Dowell, the SOFIA HAWC+ team, the SOFIA flight and ground crews, and the USRA SOFIA Project teams developed the SOFIA observatory, the HAWC+ instrument, performed the airborne observations, processed and calibrated the data, and delivered science-ready data products. D.P.C. acknowledges support funder NSF AST 18-14531, USRA SOF_4-0026 and NASA NNX15AE51G. D.S. acknowledges the support of the Bonn-Cologne Graduate School, which is funded through the German Excellence Initiative and funding by the Deutsche Forschungsgemeinschaft (DFG) via the Collaborative Research Center SFB 956 Conditions and Impact of Star Formation (subprojects C5 and C6). G.A.P.F. is partially supported by CNPq and FAPEMIG. This research has made use of data from the Herschel Gould Belt survey (HGBS) project (http://gouldbelt-herschel.cea.fr and ref. [16]).

Author contributions

T.P. led the SOFIA proposal, data analysis, interpretation of the data and the paper writing. The other authors contributed to the writing of the manuscript. D.P.C., S.R., P.C.M. and J.K. participated in the data analysis. E.L.-R. led the SOFIA data reduction. F.O.A. and G.A.P.F. conducted near-infrared polarization observations. K.S. provided the published near-infrared polarization data used in this study. J.H., K.M.M., F.N., D.S. and H.W. provided expertise in molecular cloud studies.

Competing interests

The authors declare no competing interests.

Additional information

Correspondence and requests for materials should be addressed to T.G.P.

Reprints and permissions information is available at www.nature.com/reprints.

Publisher's note Springer Nature remains neutral with regard to jurisdictional claims in published maps and institutional affiliations.